Phase Differential Angular Rate Sensor—Concept and Analysis

James D. John, Conrad F. Jakob, *Member, IEEE*, Thurai Vinay, and Lijiang Qin

***Abstract*—This paper proposes and analyzes a new differential phase angular rate (AR) sensor employing a vibrating beam mass structure that traces an elliptical path when subject to rotation due to Coriolis force. Two sensing elements are strategically located to sense a combination of drive and Coriolis vibration to create a phase differential representative of the input rotation rate. A general model is developed, describing the device operation. The main advantages of the phase detection scheme are explored, including removing the need to maintain constant drive amplitude, independence of sensing element gain factor, and advantageous response shapes. A ratio of device parameters is defined and shown to dictate the device response shape. This ratio can be varied to give an optimally linear phase difference output over a set input range, a high sensitivity around zero input rate, or a response shape not seen before, that can give maximum sensitivity around an offset from the zero-rate input. This may be exploited in an array configuration for a highly accurate device over a wide input range. A worked example shows how the developed equations can be used as design tools to achieve a desired response with low sensitivity to variation in device parameters.**

***Index Terms*—Angular rate (AR) sensor, gyroscope, microelectromechanical systems (MEMS), modeling and analysis, phase detection.**

I. Introduction

EMERGING applications require angular rate (AR) sensors that are small, cheap, and accurate. Highly accurate devices, such as fiber-optic and ring laser gyroscopes, have been developed; however, both are too expensive and not small enough for these applications [1]. The emergence of microelectromechanical systems (MEMS) has seen many AR sensors developed that have the advantage of smaller size, weight, power, and cost. These advantages allow such devices to be integrated into many mainstream applications, including jitter correction for hand held video recorders, computer and game controllers, biomedical activity monitoring, personal navigation, vehicle stabilization, and micro-unmanned aerial vehicles (MUAV) guidance. They are still less accurate than macro size conventional devices; however, micromachined AR sensor performance has improved by an order of magnitude every two years for the eight years prior to 1998 [1].

Vibrating mass [2]–[6] and vibrating ring micromachined AR sensors [7], [8] both utilize the Coriolis effect caused by rotation acting on a vibrating mass. Coriolis acceleration a_{Coriolis} acts perpendicular to a body's velocity when subject to a rotation in inertial space and is given by $a_{\text{Coriolis}} = 2v \times \Omega$ [1], where Ω is the rotation rate of the body and v is the velocity with which it is moving perpendicular to the axis of rotation (Fig. 1).

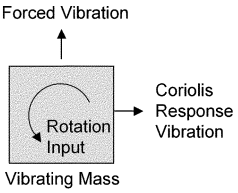

Fig. 1. Vibrating mass AR sensor principle.

A. Vibrating Mass AR Sensors

The majority of micromachined AR sensors consist of one or more mass or cantilever beams that are driven into oscillation in one axis. When subject to a rotation rate in inertial space, the mass also oscillates perpendicular to the drive axis, due to a transfer of energy between two vibration modes caused by the Coriolis force [1]. This perpendicular vibration is sensed and the resulting signal is a sine wave with amplitude modulation proportional to the input rotation.

B. Phase Detection Scheme

The first reported AR sensor to use a phase detection scheme used a trident-type three-pronged tuning fork configuration with the center arm having two capacitive sensing element below it on either side of its centerline [9]. When the arm traced an elliptical path due to the influence of Coriolis force, a phase difference representative of the input rotation, is induced in the sensor outputs. Phase detection has the advantage of removing the requirement of a constant drive amplitude, as will be shown in Section II-C.

The phase detection principle was also adopted by Yang [3], who developed a device consisting of a rectangular beam oscillated using electrostatic actuation. The electrostatic drive plate was offset to create unbalanced parasitic electrostatic forces and, consequently, a driving force that is slightly diagonal. This approach was suspected of causing nonlinearity in the results. The likely cause of this is that the drive angle will alter as the beam starts to vibrate, and the drive angle and gain factor are directly related.

In this paper, we propose a symmetrical device structure with strategic positioning of the sensing elements that has greater control over the driving force. Section II-C uncovers some novel

Manuscript received August 13, 2003; revised April 12, 2004. The associate editor coordinating the review of this paper and approving it for publication was Prof. Andrei Shkel.

The authors are with the School of Electrical and Computer Engineering, Royal Melbourne Institute of Technology (RMIT), Melbourne 3001, Vic., Australia (e-mail: james.john@ieee.org; conrad@bigharvest.com.au; thurai.vinay@rmit.edu.au; lijiang@alphalink.com.au).

Digital Object Identifier 10.1109/JSEN.2004.830962

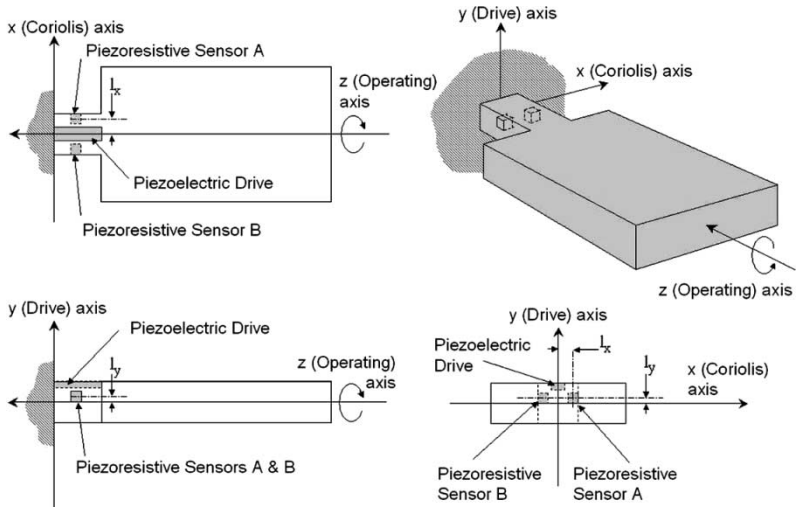

Fig. 2. Proposed device structure. Note that l_x and l_y describe the position of the piezoresistive sensor elements.

device response curves that can be achieved with the proposed device.

II. Proposed Phase-Modulated AR Sensor

A. Device Structure

The proposed device structure includes all necessary physical parameters for a mathematical analysis of the phase detection scheme. For the purpose of this analysis, it can be assumed that the device is driven into oscillation using a piezoelectric drive element and the sensor elements are piezoresistive.

The current device shown in Fig. 2 is similar in structure to Yang [3] in that it consists of a rectangular cantilever beam mass. Unlike Yang [3], it is driven into vertical oscillation using piezoelectric actuators on the beam surface near its base, to ensure that the angle at which the driving force acts on the mass remains constant, with respect to the base of the device. The drive oscillation could also be achieved using electrostatic or electromagnetic actuation; however, the use of a piezoelectric drive allows the air gap around the mass to be increased, reducing any squeeze film damping effects between electrostatic actuator surfaces. The piezoresistive sensors are located on the beam slightly offset from the centerline in the y axis, to acquire an evenly weighted ratio between drive and Coriolis vibration amplitudes. The usual tradeoff of using piezoresistors is their temperature dependent output; however, due to the amplitude independence of the phase differential scheme, this tradeoff is not applicable. Piezoresistive sensors have the advantages of being cheap, simple to fabricate, and they do not require complex conditioning electronics as required for capacitive sensing methods [10].

B. Operation

The beam mass is driven into oscillation vertically in the drive axis (y). When subject to a rotation around its operating axis (z), the mass begins oscillating in the Coriolis axis (x), due to Coriolis force acting on the mass. When the natural frequencies of the system in the x and y axes are not matched, the driving force and the Coriolis force make the mass trace an elliptical path. The piezoresistors are strategically located to sense both a component of the drive oscillation and opposite components of the Coriolis oscillation. The opposing Coriolis components cause a phase differential in the two piezoresistor sensor signals that is representative of the input rotation.

The device resolution is limited by the resolution of the phase measurement method and the amount of noise on the signals. This dependency may be reduced by reducing the operating frequency so that the phase difference is easier to measure. The device resolution can also be improved by increasing the gain factor of the device through careful parameter optimization, and by increasing the amplitude of the two sensor signals through optimum physical placement.

Although the output of the device is unaffected by variations in the drive axis amplitude, the drive amplitude must be large enough to create sufficient motion along the Coriolis axis. This can be achieved by driving the device at resonance. Typically, a phase-locked loop is used to adjust the input frequency until the drive axis output is out of phase with the input [11].

Since the system is driven very close to its resonance frequency, the drive amplitude is strongly dependent on the inherent damping in the system. To attain a sufficient drive amplitude, this damping should be kept very low. Precise control of the drive-mode amplitude is not necessary.

The placement of the sensing elements and the other design parameters are investigated in the following analysis.

C. Analysis

Typically, the effect of Coriolis force on the drive axis is negligible; therefore, the respective equations describing the accelerations in the x and y axes for a nonzero mass are [11]

$$\ddot{x} + 2\zeta_x\omega_x\dot{x} + \omega_x^2 x - 2\Omega(t)\dot{y} = 0 \tag{1}$$

$$\ddot{y} + 2\zeta_y\omega_y\dot{y} + \omega_y^2 y = \frac{f_y(t)}{m} \tag{2}$$

where $f_y(t)$ is the driving force, m is the mass Ω is the input rotation, ζ_x and ζ_y are the damping ratios, and ω_x and ω_y are the natural frequencies in their respective axes.

For this analysis, $\Omega(t)$ is assumed to be steady state and can be replaced with Ω [3]. While this is valid for the following analysis, in general, the bandwidth of this device will be similar to that of a device operating in open loop mode. The phase detection scheme relies on the mass having an elliptical path; therefore, the motion in the Coriolis axis cannot be nulled to increase the bandwidth, as is the case with many devices that operate in closed loop mode. However, one technique to increase bandwidth is to cause a slight mismatch between the drive and Coriolis axis resonant modes, which is already a prerequisite for the design of phase detection devices (i.e., u_x cannot equal zero).

Taking the Laplace transform of (1) and (2) where $X(s) = \mathcal{L}(x(t))$ and $Y(s) = \mathcal{L}(y(t))$ and solving for $X(s)$ and $Y(s)$ gives

$$X(s) = \frac{2\Omega s F_y(s)}{m\left(s^2 + 2\zeta_y\omega_y s + \omega_y^2\right)\left(s^2 + 2\zeta_x\omega_x s + \omega_x^2\right)} \tag{3}$$

and

$$Y(s) = \frac{F_y(s)}{m\left(s^2 + 2\zeta_y\omega_y s + \omega_y^2\right)}. \tag{4}$$

Piezoresistor sensors output a change in resistance due to stress

$$\frac{\Delta R}{R} = \sigma_l\pi_l + \sigma_t\pi_t \tag{5}$$

where σ_l and σ_t are the stress and π_l and π_t are the piezoresistance coefficients in the respective longitudinal and transverse directions with respect to the current flow [12].

The longitudinal and transverse stress on each sensor element can be expressed as [13]

$$\begin{aligned}\sigma_l &= \frac{2E\left(X(s)l_x + Y(s)l_y\right)}{l_z^2}\\ \sigma_t &= -\frac{2E\nu\left(X(s)l_x + Y(s)l_y\right)}{l_z^2}\end{aligned} \tag{6}$$

where ν is the Poisson's ratio, E the Young's modulus for the beam, and l_{xA}, l_{yA}, l_{zA}, l_{xB}, l_{yB}, and l_{zB} are the piezoresistor positions relative to the center of the base of the beam. Subscripts A and B have been included as inequalities may arise between the two sensor locations due to fabrication limitations; this is investigated further with the sensitivity analysis in Section II-G. Combining (5) and (6) gives

$$\frac{\Delta R_A(s)}{R_A} = \frac{2E}{l_{zA}^2}\left(l_{xA}X(s) + l_{yA}Y(s)\right)(\pi_l - \pi_t\nu). \tag{7}$$

Note that, for a greater sensor signal amplitude, the distance from the base of the beam to the sensor element l_z should be minimized to increase the stress on it. Substituting (3) and (4) into (7) gives

$$\frac{\Delta R_A(s)}{R_A} = \frac{2EF_y(s)\left(\left(s^2+2\zeta_x\omega_x s+\omega_x^2\right)l_{yA}+2\Omega s l_{xA}\right)(\pi_l-\pi_t\nu)}{ml_{zA}^2\left(s^2+2\zeta_x\omega_x s+\omega_x^2\right)\left(s^2+2\zeta_y\omega_y s+\omega_y^2\right)}. \tag{8}$$

Noting the change in sign of the Coriolis axis term, sensor B becomes

$$\frac{\Delta R_B(s)}{R_B} = \frac{2EF_y(s)\left(\left(s^2+2\zeta_x\omega_x s+\omega_x^2\right)l_{yB}-2\Omega s l_{xB}\right)(\pi_l-\pi_t\nu)}{ml_{zB}^2\left(s^2+2\zeta_x\omega_x s+\omega_x^2\right)\left(s^2+2\zeta_y\omega_y s+\omega_y^2\right)}. \tag{9}$$

Since both sensor elements are operating at similar frequencies within the sensor element bandwidth and are symmetrical in design, it is assumed that any inherent propagation delay will be small and affect both sensors equally and is, therefore, neglected. Letting α be the length ratio between l_{xA} and l_{yA}, β be the length ratio between l_{xB} and l_{yB}, u_x be the frequency ratio between ω and ω_x, and λ be the frequency ratio, between Ω and ω_x

$$\alpha = \frac{l_{xA}}{l_{yA}}, \quad \beta = \frac{l_{xB}}{l_{yB}}, \quad u_x = \frac{\omega}{\omega_x}, \quad \lambda = \frac{\Omega}{\omega_x} \tag{10}$$

the phase difference between the two sensor signals $\Delta\phi$ becomes

$$\Delta\phi = \operatorname{artan}\left(\frac{2u_x\lambda\left(u_x^2-1\right)(\alpha-\beta)}{\left(u_x^2-1\right)^2+4u_x^2\zeta_x^2+4\zeta_x u_x^2(\alpha+\beta)\lambda+4\alpha\beta u_x^2\lambda^2}\right). \tag{11}$$

Equation (11) is used to investigate sensitivity to α and β in Section II-G; however, in an ideal case, the sensor elements will be located symmetrically therefore $\beta = -\alpha$

$$\Delta\phi = \operatorname{artan}\left(\frac{4u_x\alpha\left(u_x^2-1\right)\lambda}{\left(u_x^2-1\right)^2+4\zeta_x^2u_x^2-4u_x^2\alpha^2\lambda^2}\right). \tag{12}$$

The driving force has dropped out of the equation, showing the benefit of phase detection scheme where control circuits to maintain constant driving amplitude are not required. The sensor element scaling constants have also dropped out indicating that any additional scale factor dependence, such as temperature and inequalities in distances from the base of the beam l_{zA} and l_{zB}, will not affect the phase difference between the two signals.

The final expression for the phase scheme AR sensor (12) is of the general form

$$\Delta\phi = \operatorname{artan}\left(\frac{a\lambda}{b-c\lambda^2}\right) \tag{13}$$

where

$$a = 4u_x\alpha\left(u_x^2-1\right) \tag{14}$$

$$b = \left(u_x^2-1\right)^2 + 4\zeta^2u_x^2 \tag{15}$$

$$c = 4u_x^2\alpha^2. \tag{16}$$

Upon inspection, the denominator in (13) becomes zero when $\lambda = \sqrt{b/c}$. This indicates that $\Delta\phi$ will always pass through the three points $(-\sqrt{b/c}, -\pi/2)$, (0,0) and $(\sqrt{b/c}, +\pi/2)$ when $a > 0$ and $(-\sqrt{b/c}, +\pi/2)$, (0,0) and $(\sqrt{b/c}, -\pi/2)$ when $a < 0$. Note that only a can be negative (i.e., when $u_x < 1$).

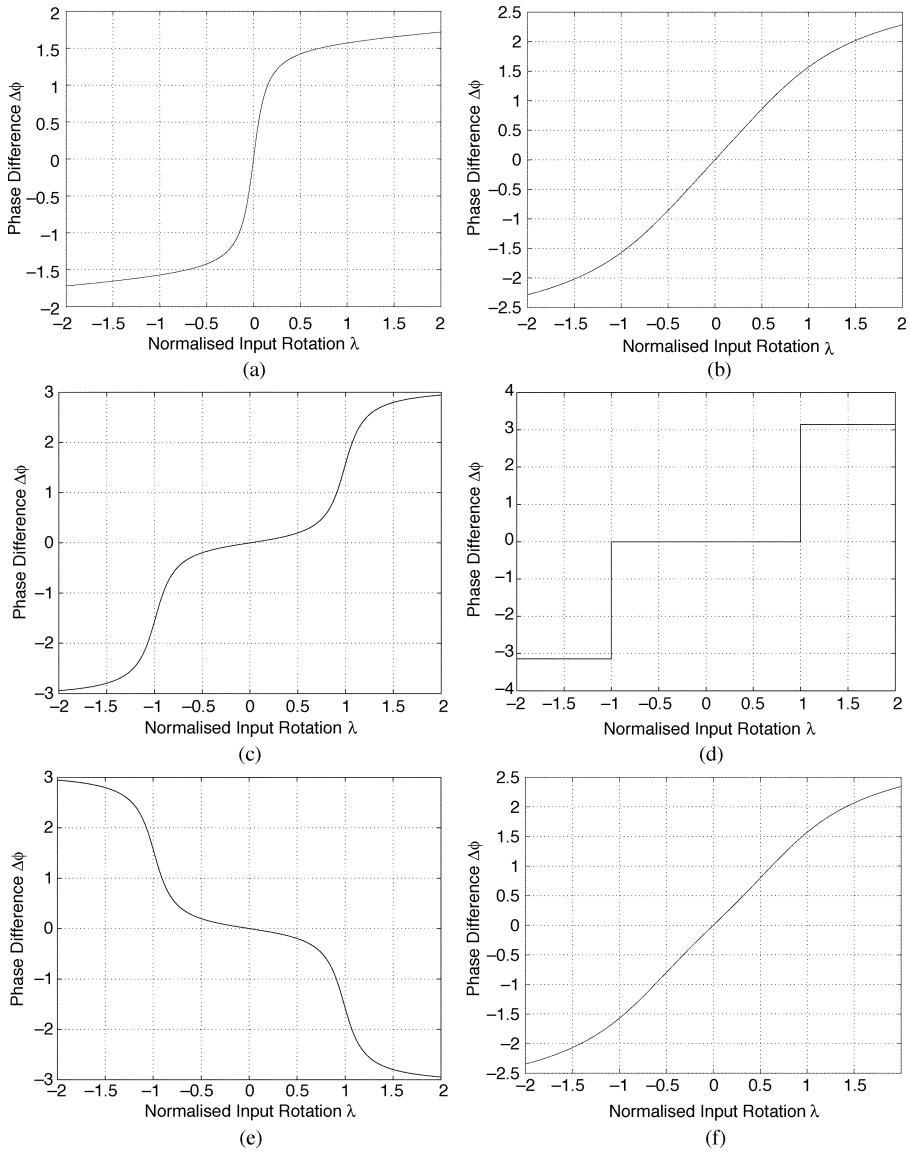

Fig. 3. Response shape determination. (a) The $|\gamma| > \sqrt{3}$ normal shape response: a high gain around the origin decreases as the value of $|\lambda|$ increases (only positive gradient case shown). (b) The $|\gamma| = \sqrt{3}$ transition shape response: the transition between the offset and normal shapes (only positive gradient case shown). (c) The $|\gamma| < \sqrt{3}$ offset shape response: response has a maximum gain, offset from the origin by λ_{Offset} in (24). (d) The $|\gamma| = 0$ zero or $\pm\pi$ phase difference response. The sudden change is due to one of the sensor elements going through zero amplitude and then inverting its phase. (e) The $\gamma < 0$ the response has a negative gradient. (f) The $|\gamma| = 1.5375$ optimal linear response: an optimally linear region in the range from $-\lambda_{\pm\pi/2}$ to $\lambda_{\pm\pi/2}$ with a gradient of approximately $2/\pi\lambda_{OP}$ (only positive gradient case shown).

Substituting (15) and (16) into $\pm\sqrt{b/c}$ gives $\lambda_{\pm\pi/2}$, the points where $\Delta\phi = \pm\pi/2$

$$\lambda_{\pm\frac{\pi}{2}} = \frac{1}{2\alpha}\sqrt{\left(\frac{u_x^2 - 1}{u_x}\right)^2 + 4\zeta_x^2}. \tag{17}$$

Equation (13) can produce two general response shapes and a point of transition between the two as can be seen in Fig. 3. The first shape Fig. 3(a) resembles a regular arctan curve that has a relatively steep section around the origin and whose gradient decreases with increasing values of $|\lambda|$. The transition Fig. 3(b) consists of a relatively straight line section that stretches between $(-\sqrt{b/c}, -\pi/2)$ and $(\sqrt{b/c}, \pi/2)$ when $a > 0$ and $(-\sqrt{b/c}, \pi/2)$ and $(\sqrt{b/c}, -\pi/2)$ when $a < 0$, before the gradient again decreases with increasing values of $|\lambda|$. The second response shape Fig. 3(c) resembles two arctan curves joined at the origin whose maximum gradient occurs at an offset in λ either side of zero.

The transition case occurs when $d^2\Delta\phi(\lambda)/d\lambda^2$ has a point of inflection at $\lambda = 0$; therefore, solving for a, b, and c gives

$$a = 0, \quad b = 0, \quad b = \frac{a^2}{3c}. \tag{18}$$

Inspection of (15) shows that $b \geq 0$; however, $b = 0$ would require the mass to be driven at resonance, destroying the elliptical nature of the movement of the mass. If the device is driven at the resonant frequency in the Coriolis axis $(\omega = \omega_x)$, then u_x becomes zero and $\Delta\phi = 0$. This destroys the elliptical path because motion in the drive and Coriolis axes will be in phase and, therefore, along a straight line through the origin. If the

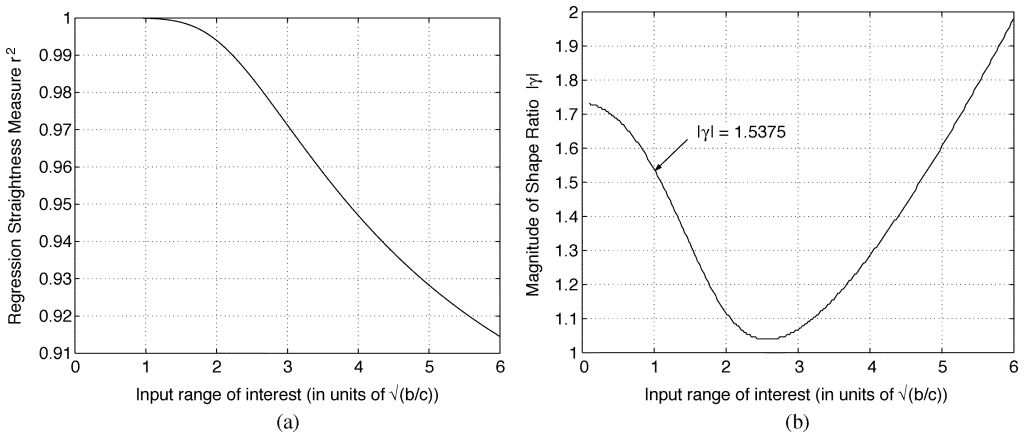

Fig. 4. Optimizing response linearity. (a) Regression r^2 values for each multiple of $\sqrt{b/c}$. (b) Corresponding values of $|\gamma|$ for each multiple of $\sqrt{b/c}$.

drive frequency is adjusted further past the resonant frequency of the Coriolis axis, then the elliptical path is created in the opposite direction (e.g., clockwise instead of anticlockwise).

Inspection of (14) also shows that $a = 0$ is nonsensical, as it would require either 1) $\alpha = 0$, which would mean that the sensing element would be positioned to only pick up the driving vibration and no Coriolis motion, 2) $u_x = 0$, meaning that mass is stationary and no driving oscillation is occurring, or 3) $u_x = 1$, the previously mentioned resonance case. All three of these cases result in $\Delta\phi = 0$ or $\pm\pi$ for all λ, as can be seen by inspecting (12).

Therefore, the transition case occurs when

$$\frac{a}{\sqrt{bc}} = \pm\sqrt{3}. \tag{19}$$

Substituting (14), (15), and (16) into (19) and simplifying gives the general expression

$$\frac{a}{\sqrt{bc}} = \frac{u_x^2 - 1}{2\zeta_x u_x} = \gamma \tag{20}$$

where γ is a variable that indicates what the general shape of the response will be (Fig. 4).

Responses plotted across a range of γ values are shown in Fig. 5. The notable sections are shown individually in Fig. 3. These show that $|\gamma| < \sqrt{3}$ gives an offset from zero response, $|\gamma| > \sqrt{3}$ gives a shape resembling a regular arctan shape, and when $|\gamma| = \sqrt{3}$, the transition between the two occurs.

When $\gamma > 0$, the response has a positive gradient, and when $\gamma < 0$, it has a negative gradient. The seemingly discontinuous points when $\gamma = 0$ can be explained simply. When $|\lambda| = \sqrt{b/c}$, one of the sensing elements will have zero amplitude resulting in an undefined $\Delta\phi$. When $\gamma = 0$ and $|\Omega| > \sqrt{b/c}$, the sensing element signal is inverted, therefore $\Delta\phi = \pm\pi$.

Equation (20) can be used as a design guideline to predict the response shape for given ζ_x and u_x values. It is interesting to note the shape of the response curve is independent of α, indicating that the shape can be scaled in λ by varying α. By definition, $u_x \geq 0$ and $0 \leq \zeta_x \leq 1$; therefore, solving (20) for u_x gives

$$u_x = \gamma\zeta_x + \sqrt{\gamma^2\zeta_x^2 + 1}. \tag{21}$$

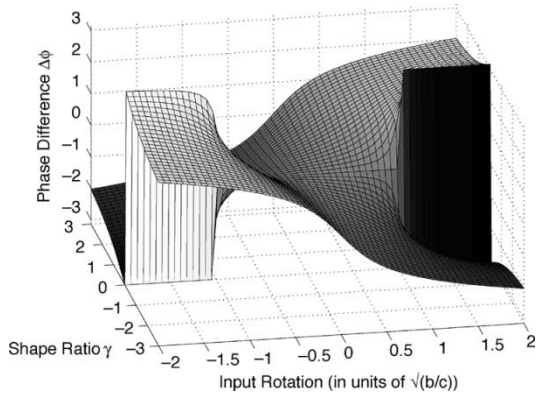

Fig. 5. Phase difference $\Delta\phi$ plotted across input AR range, for all values of γ. The γ parameter varies the response shape, with $|\gamma| < \sqrt{3}$ giving a response having maximum gradient for nonzero input rates. The gradient is positive for $\gamma > 0$ and negative for $\gamma < 0$.

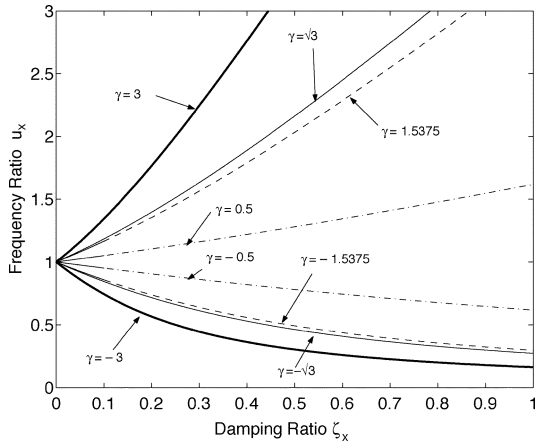

Fig. 6. Plot of u_x over ζ_x for various γ values.

The desired response shape, determined by the value of γ, can be achieved by adjusting u_x for any ζ_x value using (21) as a guide. This can physically be done by adjusting the driving frequency. For any value of ζ_x, there is always one value of u_x that will result in each response shape. Fig. 6 shows u_x plotted over ζ_x for various γ ratios. When $\zeta_x = 0$, $u_x = 1$, resulting again in the previously mentioned resonance case. If $u_x < 1$, then the response shape will have a negative gradient ($\gamma < 0$ in

Fig. 5), and if $u_x > 1$, then the response has a positive gradient ($\gamma > 0$ in Fig. 5).

The shape can then be stretched or compressed in the λ axis to achieve the desired operating range by adjusting the α parameter in (17), which can be more conveniently expressed as

$$\alpha = \frac{1}{2\lambda_{\pm\frac{\pi}{2}}}\sqrt{\left(\frac{u_x^2-1}{u_x}\right)^2 + 4\zeta_x^2}. \tag{22}$$

Substituting u_x from (21) gives α in terms of $\lambda_{\pm\pi/2}$, ζ_x, and γ

$$\alpha = \frac{\zeta_x}{\lambda_{\pm\frac{\pi}{2}}}\sqrt{\gamma^2+1}. \tag{23}$$

Noting that γ is squared, α will be the same whether the response is positive ($\gamma > 0$) or negative ($\gamma < 0$).

It should be noted that there will be tradeoffs and physical limitations on each parameter that will impose restrictions on the achievable shape and scale of the response. For example, α is limited by the fabrication resolution, and ζ_x is limited by the operating environment. As such, these limitations make good starting points for design parameters.

D. Location of Response Curve Offset

The gradient of the response curve is proportional to the sensitivity of the device and, in turn, its resolution. It was shown in Section II-C that response shapes with maximum gradients around an offset in $\lambda(\lambda_{\text{Offset}})$ are achievable when $|\gamma| < \sqrt{3}$. The size of λ_{Offset} can be found knowing that the point of maximum gradient will be a point of inflection, therefore solving $d^2\Delta\phi(\lambda)/d\lambda^2 = 0$ for λ and substituting in $a^2 = \gamma^2 bc$ from (20) gives

$$\lambda_{\text{Offset}} = \sqrt{\frac{\pm b\sqrt{4-\gamma^2}-b}{c}}. \tag{24}$$

Equation (24) has real solutions for $|\gamma| \leq \sqrt{3}$, as would be expected, and $\lambda_{\text{Offset}} = \sqrt{(b \mp \sqrt{4-\gamma^2}-b)/c}$. For small values of γ, (24) can be approximated to $\lambda = \sqrt{b/c}$, which is $\lambda_{\pm\pi/2}$ from (17).

In the opinion of the authors, an AR sensor with offset operating point is novel and not described previously in the literature. Such a device could be used to give a steeper response gradient at ARs within a range offset from zero, improving the output resolution in this range, and with shallower response gradient around zero. This variation in response gradient with AR is useful where the device rotates constantly and measures deviations from the constant rotation, or where measurements are expected within a narrow range of ARs. One possible application for this may be on a vehicle, where higher rotation rates would need stabilization system assistance, requiring a device with higher accuracy at higher rates.

A more interesting application is using an array configuration where multiple overlapping responses are used, each having a high resolution around their respective operating ranges, with sensor outputs combined to give a high resolution output over a wide input range. This type of configuration would be more efficient if all the masses in the array used common drive circuitry and possibly sensing circuitry. From (17), α influences the offset of the operating range. Therefore, multiple responses curves with overlapping high sensitivity ranges can be achieved by incorporating multiple pairs of sensing elements, each with different α values, on a single vibrating mass. It may also be worth investigating if one mass could be used with a varying drive frequency to focus the operating point.

E. Optimizing Response Linearity

The transition shape gives a relatively straight section between $\pm\sqrt{b/c}$; however, it is not necessarily the straightest response achievable between these two points. Since γ governs the general shape of the response, it was hypothesised that there would be a corresponding value for γ that would give the straightest response over a range of interest of λ. Algebraic measures of the linearity were intractable, so this was verified using regression r^2 values as a measure of linearity and plotting the maximum achievable r^2 against the range of interest of λ in units of $\sqrt{b/c}$. This can be seen in Fig. 4(a). It shows that the r^2 values are very close to 1 for ranges of interest up to $\sqrt{b/c}$ before trailing off, indicating that an almost linear response ($r^2 = 0.999\,91$) can be achieved for ranges within $\pm\sqrt{b/c}$. Fig. 4(b) shows the values of γ that will achieve the maximum r^2 values. For example, $\gamma = 1.5375$ will maximize linearity over a range of $\pm\sqrt{b/c}$. This optimized shape is shown in Fig. 3(f). The bounds of the linearised region are given by $\lambda_{\pm\pi/2}$ in (17).

It should be noted that a device does not necessarily require a linear response if the response is known. In some cases, nonlinearity may be an advantage. However, if a linear response can be achieved, it may save additional output-scaling signal-conditioning electronics. It should also be noted that the most linear response over a range of interest may not necessarily give the greatest gradient over the same range; however, a response with a greater gradient may still have acceptable linearity.

The next section gives a worked example that shows how the various derived equations can be used to choose parameter values to achieve the desired response shape.

F. Design Example

As yet, a prototype differential phase AR sensor has not been developed, but fabrication of a device is planned for future work. However, early Simulink simulations of the physical device operation yield the responses predicted by the mathematical model presented in 12.

An AR sensor is required that gives a positive linear type response over $\pm 500^\circ$/s given that $\zeta_x = 0.05$ and $\omega_x = 1000$ Hz

When $\gamma = \pm 1.5375$ in (20), the most linear response is achieve over the range $\pm\sqrt{b/c}$. Therefore, from (21)

$$u_x = +\sqrt{1.5375^2 \times 0.05^2 + 1} \pm 1.5375 \times 0.05 \tag{25}$$

$$u_x = 0.9261, 1.0798. \tag{26}$$

The response will have a positive gradient when $u_x > 1$, therefore

$$\omega = 1079.8 \text{ Hz}. \tag{27}$$

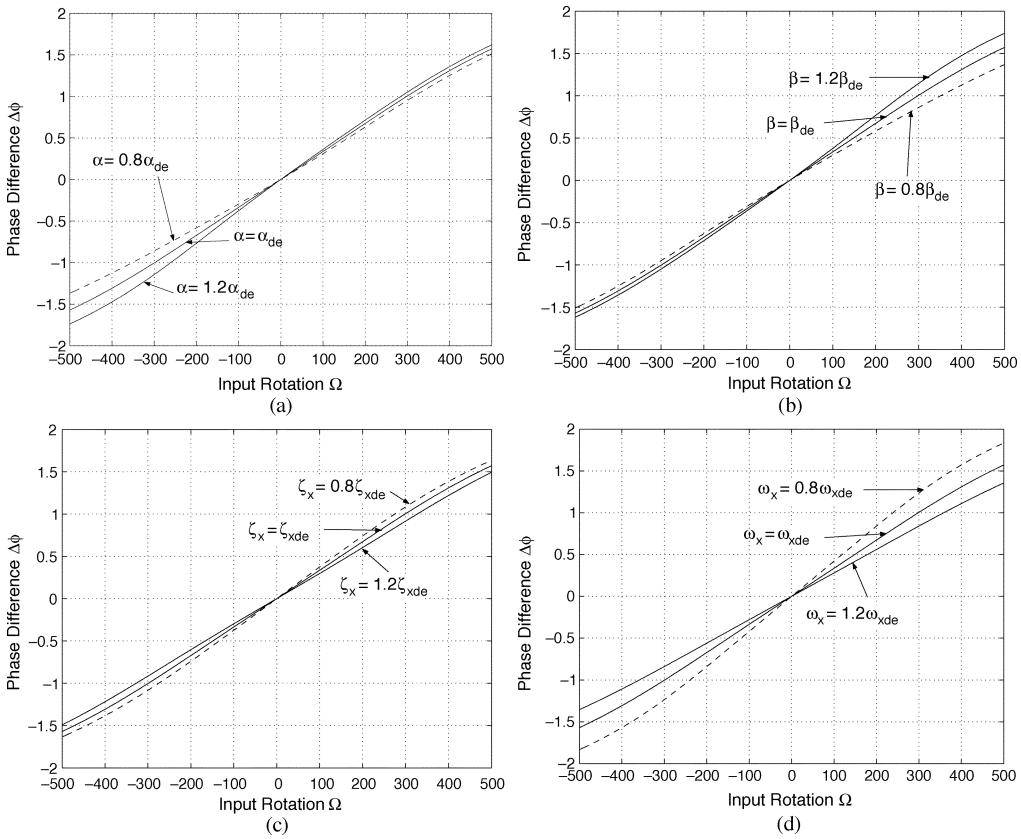

Fig. 7. Sensitivity results for the design example. (a) Sensitivity to 20% variation in α shown either side of the design example responses for $u_x = 1.0798$. (b) Sensitivity to 20% variation in β shown either side of the design example responses for $u_x = 1.0798$. (c) Sensitivity to 20% variation in ζ_x shown either side of the design example responses for $u_x = 1.0798$. (d) Sensitivity to 20% variation in ω_x shown either side of the design example responses for $u_x = 1.0798$.

Note that for a negative response $u_x = 0.9261$ would be used and treated the same way.

Given $\lambda = \Omega/\omega_x$

$$\lambda_{\pm\frac{\pi}{2}} = \frac{\pm 500^\circ/\text{s} \times \frac{\pi \text{ rad}}{180^\circ}}{1000 \text{ Hz} \times 2\pi \text{ rad}} = 0.0014 \tag{28}$$

and using (23), $\alpha = \pm 66.0274$.

The design example response for $u_x = 1.0798$ can be seen in each plot in Fig. 7. The response is almost linear ($r^2 = 0.99991$), and it has phase differential of approximately $0.18^\circ/^\circ/\text{s}$ in the range of $\pm 500^\circ$, as compared to Yang [3], which gave a phase change of $0.152^\circ/^\circ/\text{s}$ in the range of $\pm 120^\circ$ with a driving frequency of 700.6 Hz. This is a major improvement, due in part to using the phase differential between two sensor signals instead of the phase shift of a single sensor signal [3].

G. Sensitivity Analysis

Due to the large number of parameters in the model, an exhaustive algebraic exploration of model sensitivity is intractable, therefore numerical substitution will need to be used for each design case. A sensitivity analysis was carried out for the design example above using (11) and (12), for $\beta = -\alpha_{de} \pm 20\%$, $\zeta_x = \zeta_{\pm} 20\%$, and $\omega_x = \omega_{xde} \pm 20\%$, where the subscript de indicates the design example values. The results are shown in Fig. 7. It can be seen that with a 20% parameter deviation in each case the deviation in output ranges from approximately 5% for ζ and 20% for ω_x. It should be noted that these results are valid for the design example and will vary for different parameter values.

When ω_x is varied, the frequency ratio u_x is assumed to be maintained by varying the driving frequency ω. This is a critical issue as the values of u_x to achieve the desired response are very precise. However, a constant u_x can be achieved by monitoring the phase difference between the motion in the drive axis (Sensor A + Sensor B) and the Coriolis axis (Sensor A − Sensor B), which gives an indication of u_x and varying the drive frequency ω accordingly. This could be the basis of a self-calibration system for the device. Altering the driving frequency ω to maintain constant u_x has no effect on the general shape of the response; however, it does affect its scale in the input axis linearly since $\lambda = \Omega/\omega_x$ in (17). This can be compensated for in the final scale factor of the output.

III. Conclusion

A new phase differential AR sensor has been proposed. Analysis has shown it can be designed to give response shapes relatively linear for a given input range ($r^2 \approx 1$), to give high sensitivity around zero, or high sensitivity around input rates offset from zero. The not-seen-before "offset from zero" case ($|\gamma| < \sqrt{3}$) may be exploited in an array configuration to give a device with high sensitivity over a wide range of input rotation rates. Sensitivity analysis of a design example has shown low

sensitivity to variation in device parameters when the ratio between the driving frequency and the natural resonant frequency in the sense axis is maintained. As an alternative to amplitude detection for AR sensing, a phase differential scheme possess various other advantages. Phase differential is independent of driving amplitude, removing the need for complex amplitude control circuits. Any scale factor influence on the sensing element, such as temperature dependence, does not affect the phase differential output.

REFERENCES

[1] N. Yazdi, F. Ayazi, and K. Najafi, "Micromachined inertial sensors," *Proc. IEEE*, vol. 86, pp. 1640–1659, Aug. 1998.

[2] S. E. Alper and T. Akin, "A symmetric surface micromachined gyroscope with decoupled oscillation modes," *Sens. Actuators A*, vol. 97–98, pp. 347–358, 2002.

[3] H. Yang, M. Bao, H. Yin, and S. Shen, "A novel bulk micromachined gyroscope based on a rectangular beam-mass structure," *Sens. Actuators A*, vol. 96, no. 2–3, pp. 145–151, 2002.

[4] H. Luo, X. Zhu, H. Lakdawala, L. Carley, and G. Fedder, "A copper cmos-mems z-axis gyroscope," in *Proc. 15th IEEE Int. Conf. Microelectromechanical Systems*, 2002, pp. 631–634.

[5] H.-T. Lim, J.-W. Song, J.-G. Lee, and Y.-K. Kim, "A few deg/hr resolvable low noise lateral microgyroscope," in *Proc. 15th IEEE Int. Conf. Microelectromechanical Systems*, 2002, pp. 627–630.

[6] S. Kim, B. Lee, J. Lee, and K. Chun, "A gyroscope array with linked-beam structure," in *Proc. 14th IEEE Int. Conf. Microelectromechanical Systems*, 2001, pp. 30–33.

[7] F. Ayazi and K. Najafi, "A harpss polysilicon vibrating ring gyroscope," *J. Microelectromech. Syst.*, vol. 10, no. 2, pp. 169–179, 2001.

[8] G. He and K. Najafi, "A single-crystal silicon vibrating ring gyroscope," in *Proc. 15th IEEE Int. Conf. Microelectromechanical Systems*, 2002, pp. 718–721.

[9] M. Abe, E. Shinohara, K. Hasegawa, S. Murata, and M. Esashi, "Trident-type tuning fork silicon gyroscope by the phase difference detection," in *Proc. 13th IEEE Int. Conf. Microelectromechanical Systems*, 2000, pp. 508–513.

[10] M. Kraft, "Closed Loop Digital Accelerometer Employing Oversampling Conversion," Ph.D. dissertation, School of Engineering, Coventry Univ., Coventry, U.K., 1997.

[11] R. Leland, "Adaptive tuning for vibrational gyroscopes," in *Proc. 40th IEEE Conf. Decision and Control*, vol. 4, 2001, pp. 3447–3452.

[12] M. J. Madau, *Fundamentals of Microfabrication: The Science of Miniturization*, 2nd ed. Boca Raton, FL: CRC, 2002.

[13] R. C. Hibbeler, *Statics and Mechanics of Materials*. Englewood Cliffs, NJ: Prentice-Hall, 1993.

James D. John received the B.Eng. degree (Hons.) in mechatronics from Deakin University, Geelong, Australia, in 2000. He is currently pursuing the Ph.D. degree in microelectromechanical systems, focusing on AR sensing, at the Royal Melbourne Institute of Technology, Melbourne, Australia.

He was with Motorola at their Adelaide, Australia, software development center.

Mr. John was awarded the Sir Alfred Deakin Medal by Deakin University.

Conrad F. Jakob (M'00) received the Ph.D. degree in digital signal processing from the Royal Melbourne Institute of Technology (RMIT), Melbourne, Australia, in 2000.

His professional and research experience has included being a Research Fellow at RMIT University and a Research Engineer in the fields of computer graphics and digital signal processing. He is currently working privately.

Thurai Vinay received the B.S. degree in mechanical engineering from the University of Ceylon, Colombo, Sri Lanka, in 1968 and the Ph.D. degree from the Department of Electronic and Electrical Engineering, University of Birmingham, Birmingham, U.K., in 1974.

He is currently a Senior Lecturer in the School of Electrical and Computer Engineering, the Royal Melbourne Institute of Technology, Melbourne, Australia. In recent years, he has been associated with collaborative research projects with industry in the area of MEMS.

Lijiang Qin was born in 1962 in Shanxi, China. He received the B.S. degree in electrical engineering from the Taiyuan Institute of Technology, Taiyuan, in 1982, the M.Eng. degree from the Harbin Institute of Technology, Harbin, China, in 1985, and the Ph.D. degree from the Royal Melbourne Institute of Technology, Melbourne, Australia, in 2001.

His professional and research experience has included work at Southeast University on industry application of advanced control systems and the Royal Melbourne Institute of Technology, Melbourne, Australia, where he worked on the design and control of magnetic bearings and magnetic MEMS design and simulations. He is currently working on control system design and DSP implementation for high-precision CNC tools.